Energy Storage Materials 42 (2021) 22–33

Contents lists available at ScienceDirect

Energy Storage Materials

journal homepage: www.elsevier.com/locate/ensm

# Natural "relief" for lithium dendrites: Tailoring protein configurations for long-life lithium metal anodes

Xuewei Fu[a], Ryan Odstrcil[a], Munan Qiu[a,b], Jin Liu[a,*], Wei-Hong Zhong[a,*]

[a] School of Mechanical and Materials Engineering, Washington State University, Pullman, WA 99164, USA
[b] State Key Laboratory of Organic-Inorganic Composites, Beijing University of Chemical Technology, Beijing 100029, China

ARTICLE INFO

*Keywords:*
Zein
Molecular configuration
Lithium dendrite relief
Denaturant
Ion interaction

ABSTRACT

Rechargeable lithium metal batteries (LMBs) are faced with concerns of safety and short lifespan because of the uncontrollable growth of lithium (Li) dendrites. Natural biomolecules enriched with diverse polar groups are likely to have high lithiophilicity, showing the potential to suppress the dendrite growth. However, besides the chemical compositions, their structural diversities from nature induce notable impacts on the functions, which has not been studied yet. Here, through experiments and molecular simulations, we discover a natural "relief" for Li dendrites, zein protein, and successfully strengthen its dendrite-suppressing ability by tailoring its configurations to achieve long-life Li anodes. The "strong relief configuration" (SRC-Zein) is generated via drastically unfolding and opening the compact protein structure using a powerful denaturant. Modifying the separator by SRC-Zein results in excellent electrolyte wettability, higher ionic conductivity (2.0 mS/cm), and higher $Li^+$ transference number (0.68), compared with the less unfolded protein. These important properties play the synergistical role in homogenizing the ion deposition and inhibiting the nucleation/growth of Li dendrites. As a result, the symmetrical Li/Li cell exhibits exceptional cycling stability for more than 1400 h at 2 mA/cm$^2$. Furthermore, the half-cell with the SRC-Zein modified separator shows significant enhancement in capacity, cycle stability, and rate performance.

## 1. Introduction

The widespread implementation of electric transportation increases the needs for battery systems that can supply higher energy in a reduced volume/mass. Lithium (Li) metal is considered as a "Holy Grail" anode for high-energy-density batteries, as it features ultrahigh theoretical capacity (3860 mAh/g), the lowest electrochemical potential (-3.04 V vs. a standard hydrogen electrode), and low bulk density (0.59 g/cm$^3$) [1–2]. However, before making the Li anode a viable technology, a number of obstacles must be overcome, the greatest of which are the poor safety and short cycle life. The unstable Li/electrolyte interface along with the uncontrollable growth of Li dendrites during the repetitive Li plating/stripping processes is the root of the problems [3–4]. The sharp Li dendrites can puncture the separator, leading to an internal short-circuit and battery failure. Meanwhile, the dendrites can break the solid electrolyte interphase (SEI) layer and consume more electrolytes, which severely degrade the Coulombic efficiency and capacity retention [5–6]. To address the above issues, it is critical to stabilize the Li/electrolyte interface for suppressing the growth of Li dendrites.

The problematic surface morphologies (grooves, scratches, etc.) of the Li anode and the anisotropic distribution of $Li^+$ flux in the electrolyte (ions concentrate near separator pores) are the primary factors generating an unstable or uneven Li/electrolyte interface [7–8]. Considerable research activities have been undertaken to infiltrate Li into 3D or lithiophilic host materials/current collectors [9–11]. These efforts are effective to stabilize the Li/electrolyte interface via reducing the local current density and/or governing the distribution of $Li^+$ flux. However, the Coulombic efficiency in initial cycles is often very low and the volumetric/gravimetric energy still needs to be improved. As an essential interfacial component that intimately links with the Li anode, the separator generates a profound impact on Li/electrolyte interface. Separator modification shows advantages in fabrication ease, adaptability with current battery production, and compatibility with high energy batteries compared with nanostructure design of the Li anode. Therefore, enabling the separator to form a stable Li/electrolyte interface and thereby suppress the dendrite growth has shown great potential for the realization of high energy, safe, and stable Li metal batteries (LMBs).

It has been well established that the inhomogeneous deposition of $Li^+$ essentially leads to dendrite nucleation [12–13], such that designing separators that can guide uniform ion deposition becomes the key solution to increasing the energy, safety, and lifespan of LMBs. Modifiers with ordered pore structures (e.g., metal-organic frameworks (MOFs) [14–15], nanoporous anodic aluminum [16], etc.) or favorable lithiophilicity (e.g., chitin[17], dopamine [18], Mg [19], etc.) being coated

* Corresponding authors.
*E-mail addresses:* jin.liu2@wsu.edu (J. Liu), katie_zhong@wsu.edu (W.-H. Zhong).

https://doi.org/10.1016/j.ensm.2021.07.010
Received 2 June 2021; Received in revised form 6 July 2021; Accepted 12 July 2021
Available online 17 July 2021

on separators were proved effective for making the $Li^+$ deposit in a more uniform manner. However, the migration of $Li^+$ can be impeded by the free anions that travel in an opposite direction, especially under high current densities. This drives the $Li^+$ flux to distribute unevenly, generating a space-charge region near the anode which initiates the nucleation of Li dendrites [20–21]. Therefore, homogenizing $Li^+$ flux and eliminating the disturbance from anions (i.e., tethering the anions) are highly desired. To this end, various modifiers working in size sieving or non-covalent binding with anions have been added on separators, such as $Li_{6.4}La_3Zr_{1.4}Ta_{0.6}O_{12}$ (LLZTO) [22], amino-functionalized titanium-based MOF ($NH_2$-MIL-125(Ti)) [14], Al-doped zeolite [23], etc. These additions greatly push forward the progress of separator engineering towards the success of advanced LMBs.

As revealed above, an "ideal" separator modifier should be able to depress migration of anions and homogenize $Li^+$ flux without hindering the ion-transport. Besides a rational structure design, careful tailoring of molecular interactions is significant to achieve this goal. Gifted from nature, natural biomolecules, which possess rich molecular interactions from compositional/structural diversities, provide a promising alternative and have been increasingly receiving interest nowadays [24–25]. Among them, cellulose-derived separators (bacteria cellulose, lignocellulose, etc.) [8,26–28] obtaining abundant polar groups (particularly -OH) and good lithiophilicity have been intensively studied to regulate the distribution of $Li^+$ flux and promote the transport of $Li^+$. Another important class of biomolecules, proteins, characterized by compositional and structural complexity, emerge as a more interesting but extremely complicated system that may generate unique effects on the Li anode via richer interactions. For instance, Wu et al. [29] used sericin protein composed of both lithiophilic (-OH and -COOH) and anionphilic ($-NH_2$) polar groups to stabilize the ion deposition and suppress the dendrite growth. Wang's group [30] applied fibroin protein to cover the Li dendrite "tip" via polar groups (-NH and C=O), so as to prevent the dendrite proliferation. Looking at previous efforts, one concludes that in the electrochemical community the utilization of biomolecules, particularly proteins, still rests on the consideration of chemical compositions. It is well known that the intrinsically versatile structures of biomolecules generate strong impacts on their properties/functions in a biological environment [31–32]. This is analogous to the condition inside a "battery environment", which has not been studied thus far. Deciphering the structural effects on the molecular interactions with electrochemical species, such as electrolyte ions, will significantly promote the prediction and selection of biomolecules from the vast database of nature for maximizing their function to stabilize the Li anode.

Herein, through experiments and molecular simulations, we explore a natural Li-dendrite "relief", zein protein, and try to carefully tailor its molecular configurations. Via vigorous unfolding of zein molecular structure, we successfully discover a "strong relief configuration" (denoted as SRC-Zein) that is more effective in suppressing Li dendrites than the less unfolded zein. Growing the SRC-Zein on a separator, electrolyte wettability, ionic conductivity (2.0 mS/cm) and $Li^+$ transference number (0.68) are all boosted. As a result, the symmetrical Li/Li cell with the SRC-Zein modified separator delivers a markedly prolonged cycle life for more than 1400 h. Furthermore, the resulting $LiMn_2O_4$/Li (LMO/Li) half-cell demonstrates obviously enhanced capacity, cycle stability, and rate capability.

## 2. Results and discussion

In this study, we explore a "relief" for Li dendrites from nature, i.e., zein protein, and modulate its molecular configurations to achieve a potent suppression of Li dendrites from the root. **Fig. 1a** depicts the design concept and the strategy to manipulate the zein molecular configurations for generating the "strong Li-dendrite relief". Natural zein is a complex biomacromolecule with four-level of folded structures that encompass considerable amino acid side groups [33]. The molecular weight of zein used in this study is analyzed by sodium dodecyl sulphate-polyacrylamide gel electrophoresis (SDS-PAGE) in **Figure S1**, which is determined to be 20 – 25 kDa ($\alpha$,$\gamma$-zein) and 37 – 50 kDa ($\gamma$-zein) [34]. Via different unfolding approaches, the zein configurations are carefully adjusted, which impacts the suppression of Li dendrites. As shown, we apply two denaturants, that is, aqueous ethanol (aq. EtOH) and aqueous acetic acid (aq. HAc), exhibiting varied unfolding strength to tailor the molecular configurations in the transient unfolding stage. By using the aq. EtOH as a denaturant, its limited unfolding ability yields a relatively close configuration, i.e., "poor relief configuration" (denoted as PRC-Zein). In contrast, the aq. HAc drastically unfolds the native zein by breaking more intermolecular bonds, leading to a "strong relief configuration" (denoted as SRC-Zein). Growing the SRC-Zein on a separator, the suppression of Li-dendrite nucleation/proliferation and the facilitation of $Li^+$-transfer are simultaneously strengthened when compared to the PRC-Zein.

Through a series of all-atom molecular dynamics (MD) simulations that are performed to explore the configurations of zein being unfolded by different denaturants, the time evolution of the $\alpha$-helix length of zein in simulations up to 400 ns are shown in **Fig. 1b**. As illustrated by the figure, a comparison of the helix lengths emphasizes that the zein in aq. EtOH does not unfold to the same degree as in aq. HAc. However, upon further examination of other metrics for the simulations, such as the radius of gyration (Rg) and root mean square deviation (RMSD) in **Figure S2**, it becomes apparent that both denaturants cause zein to unfold and become more expansive. Rg is a useful metric for measuring the extent to which the tertiary structure of zein is undermined, as the breaking of intermolecular bonds such as salt bridges or disulfide bonds allows the protein configuration to become more expansive. The RMSD is used to evaluate whether the zein has been simulated for a long enough time that the maximum degree of denaturation has been achieved; when the zein has been denatured to the fullest extent capable by the denaturant, the RMSD no longer increases and remains relatively constant. For the zein in aq. EtOH, the protein quickly unfolds from the beginning of the simulation, leading to an increase in Rg and RMSD within the first 200 ns. However, the zein structure then becomes stable in a relatively compact structure by 400 ns, indicating that further MD simulation is not necessary. The zein in aq. HAc undergoes a slower unfolding process, but the zein secondary structure ($\alpha$-helices and $\beta$-sheets) is substantially undermined by 400 ns, causing a configuration expansion that increases the Rg and RMSD. Thus, even though both denaturants result in more expansive zein configurations, the zein in aq. HAc has a decreased length of helices, depicted in **Fig. 1d**, which indicates a more flexible and expanded random coil structure than the zein in aq. EtOH, as shown in **Fig. 1c**. This is the basic element that generates the varied effects on suppressing dendrites, which will be discussed in detail later.

To further investigate zein configurations, we measure the complex viscosity of the zein solutions with different denaturants in **Fig. 2a**. It is well known that the viscosity of proteins reflects the denaturation or unfolding degree of the protein molecules [35–36]. In general, proteins with a higher degree of denaturation show greater viscosities because of the more expansive and disentangled protein coils. As clearly shown, the complex viscosity of the SRC-Zein solution is greater than that of the PRC-Zein solution throughout the sweep frequency range, which suggests that the SRC-Zein shows a more expansive molecular configuration due to a higher unfolding degree. The particle size of zein in the two solutions also verifies this result. In **Fig. 2b**, the SRC-Zein shows an average particle size of 389 ± 35 nm, which is smaller than that of the PRC-Zein (456 ± 49 nm). This result indicates that the aq. HAc denaturant more effectively undermines the big zein particles in its native state and disrupts more of the protein structure compared to aq. EtOH.

The XRD pattern in **Fig. 2c** shows that the pristine zein has a highly crystalline structure. There is a sharp $2\theta$ peak located at 19.7° due to the $\alpha$-helix structure in the native protein [37–38]. The ordered crystalline structure conceals numerous functional groups inside the protein chains, such as -COOH, -C=O and $-NH_2$, etc., weakening the functional activities of zein [39]. Therefore, the unfolding process is critical for

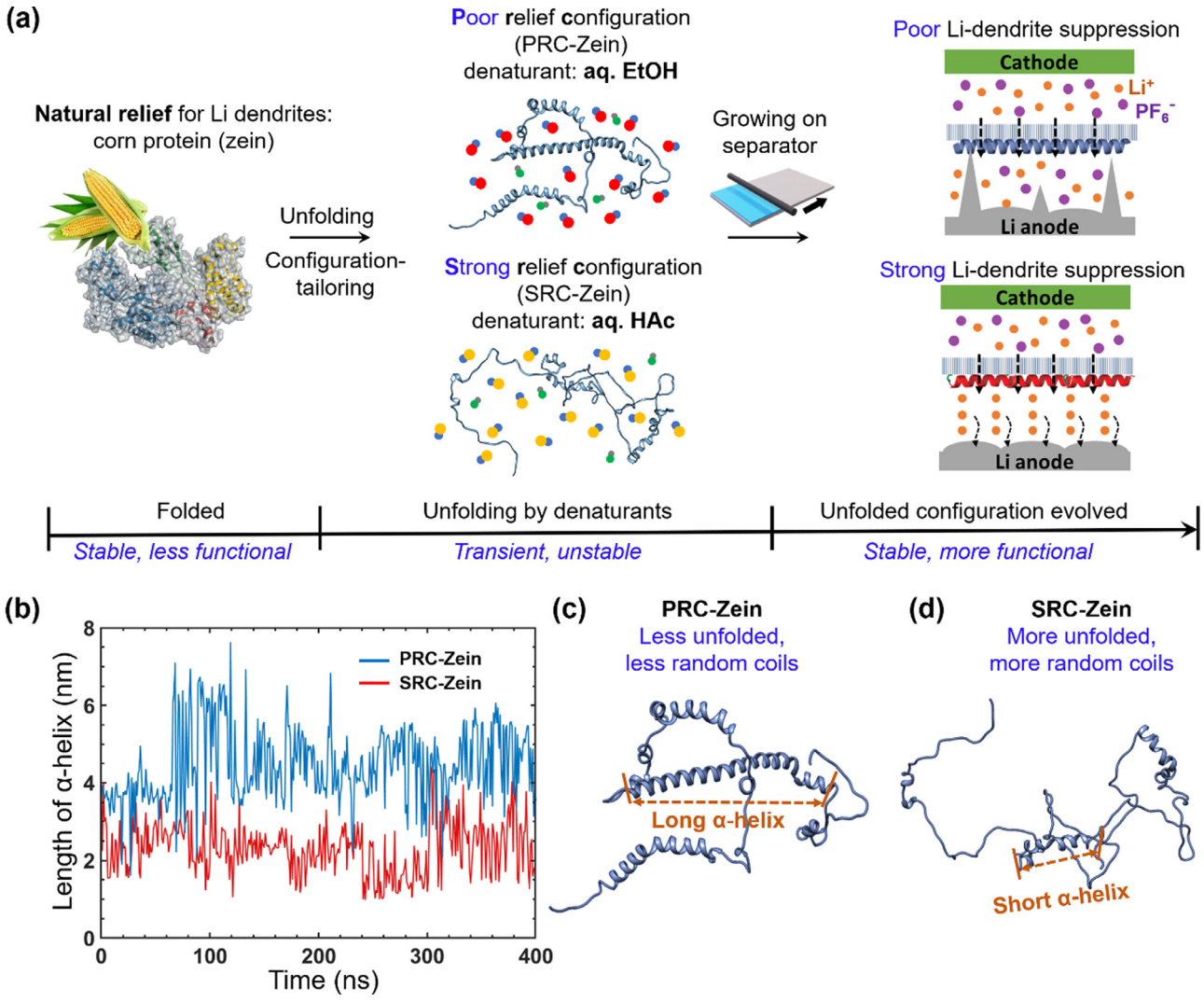


**Fig. 1.** Tailoring protein configurations to suppress Li dendrites. (a) Schematic of the strategy to tailor the protein configurations by various denaturants and the configurational effects on suppressing Li dendrites. (b) Time evolution of total length of the $\alpha$-helix of PRC-Zein and SRC-Zein via molecular simulations. (c) PRC-Zein and (d) SRC-Zein after being unfolded.

disrupting the crystalline structure, expanding the chains, and exposing the functional groups outside. As can be seen for PRC-Zein and SRC-Zein, the peak intensities are notably decreased and the peak widths become broader, indicating a reduced crystallinity for both cases due to the unfolding effect. To further understand how the denaturants affect the unfolded structure, XPS measurement is carried out and the results are shown in Fig. 2**d**. Two distinct N peaks can be found for both PRC-Zein and SRC-Zein; the fitting results are illustrated accordingly. The peaks at 400.1 eV and 399.5 eV are attributed to amide $N/NH_3^+$ and $NH_2$, respectively [40]. The increased content of amide $N/NH_3^+$ of SRC-Zein is due to the protonation by HAc in the unfolding process compared with the PRC-Zein and pristine zein (**Figure S3**). The above results imply that the denaturant plays a vital role in the unfolding process and the resulting zein configurations. Proteins possess four levels of structures (primary, secondary, tertiary and quaternary structures) [41]. The tertiary structure is formed and stabilized by H-bonding, salt bridges and disulfide bonds [42]. The unfolding process is able to destroy the high-level of structures by breaking these bonds. It is reported that acids and alcohols can undermine secondary and tertiary structures [43]. Acids (e.g., HAc) alter the charges on the protein side chains and convert the $-COO^-$ ion to the -COOH group, which prohibits the ionic interaction between the charged side chains (i.e., salt bridges). Meanwhile, HAc changes the protonation status and restricts the participation of amino acid residues in forming H-bonding. Polar EtOH forms H-bonding with the protein and hence disrupts the intramolecular H-bonding within the protein but is less capable of breaking the salt bridges. As illustrated in Fig. 2**e and f**, both aq. EtOH and aq. HAc can destroy the H-bonding of zein, but salt bridges can only be broken by aq. HAc. Consequently, by using aq. HAc as the denaturant, zein becomes more unfolded as illustrated in Fig. 2**f**. The above results are consistent with the molecular simulations that the SRC-Zein exhibits a more expansive and more flexible configuration.

The unfolded zein (PRC-Zein and SRC-zein) is grown on one side of the separator surface, which will be placed adjacent to the Li anode to stabilize the Li/electrolyte interface. As shown in Fig. 3**a and b**, the SRC-Zein exhibits an ordered spherical structure with an average diameter of ca. 315 nm. The protein nanospheres ensure the penetration of liquid electrolytes without causing noticeable resistance. The as-unfolded SRC-Zein exhibits a spherical structure in **Figure S4** with a diameter of about 50 nm. The particle size is much smaller than that of the protein coated on the separator (~300 nm), because the protein solution was deeply diluted for TEM observation and the agglomeration of protein nuclei was reduced accordingly. Similarly, the PRC-Zein also shows a spherical structure in **Figure S5** but its average diameter, which is

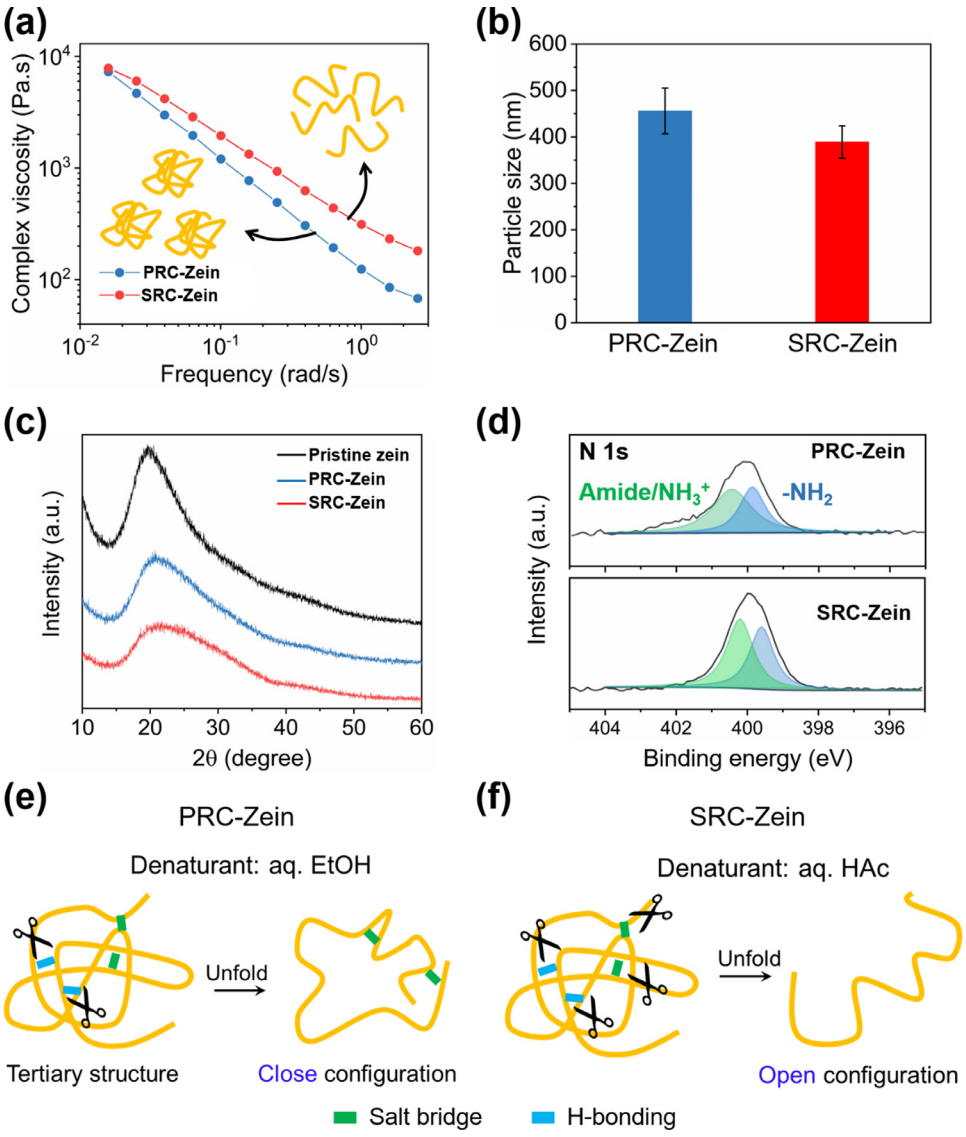


**Fig. 2.** Studies on molecular configurations of zein unfolded by different denaturants. (a) Complex viscosity versus angular frequency and (b) particle size of zein with various configurations in solution state. (c) XRD patterns of zein with various configurations compared with pristine zein. (d) High-resolution N 1s XPS spectra of zein with various configurations. Schematics of unfolding zein by (e) aq. EtOH and (f) aq. HAc leading to close and open configurations, respectively.

about 273 nm, is slightly smaller than that of the SRC-Zein. This is possibly because EtOH, with a lower boiling point (78.37 ˚C) than that of HAc (117.9 ˚C), is more volatile and evaporates faster, thus reducing the size of protein nuclei. From the cross-sectional SEM images in **Figure S6a and b**, the thickness of the PRC-Zein and SRC-Zein coating layers is ca. 7 and 9 μm, respectively. Both of the coating layers exhibit certain and similar adhesion force to the separator; the average adhesion force of PRC-Zein and SRC-Zein layers is ca. 0.76 and ca. 0.80 N, respectively (**Figure S6c**). Besides, porosity is a vital element for the coating quality, and PRC-Zein has a porosity of 40.1 ± 0.8%, which is slightly higher than that of the SRC-Zein (38.3 ± 0.5%). These results imply that the two protein coating layers have analogous structural properties.

The FTIR and XPS spectra are used to investigate the surface signal changes of the zein-modified separators. Compared with the pristine commercial separator (denoted as CS), the PRC-Zein and SRC-Zein coated separators show three new characteristic peaks at 1108, 1541 and 1654 $cm^{-1}$, which are attributed to C-O stretching, N-H bending (amide II) and C=O stretching (amide I) from zein, respectively (**Figure S7a**) [44–45]. Meanwhile, in **Figure S7b**, the XPS spectrum of CS only presents one C1s peak from the backbone structure of polyethylene (PE) and polypropylene (PP). After being coated by PRC-Zein or SRC-Zein, additional O1s and N1s peaks emerge, which results from the protein structure. Specifically, the O1s peak mainly originates from C=O, -OH and C-O groups, and the N1s peak consists of -NH and C-N groups [46]. The results prove that zein nanospheres are successfully coated on the separator and make the surface more polar, which is favorable for the permeation of liquid electrolytes and the facilitation of ion transfer, as discussed below.

Commercial polyolefin separators are highly hydrophobic and suffer from poor wettability to liquid electrolytes, which is a critical drawback that degrades the rate performance [47–48]; increasing the surface polarity of separators is beneficial for electrolyte uptake and ion transfer, especially at high current rates. To gain a deeper insight into the effects of zein configurations on the ion transfer kinetics, we characterize the chemical compositions of zein using an amino acid analyzer. Zein embeds nearly all kinds of amino acids, which means lithiophilic (-C=O and -COOH) and anionphilic ($-NH_2$) polar groups are richly found in it. Its potential to interact with electrolyte ions is hence expected and a better utilization of these chemical groups may improve the interactions and then the electrochemical performance. As shown in **Fig. 3c**, the polar amino acids such as Glu., Pro., Ser., etc. account for 54.6% of zein. Therefore, it is expected that exposing those polar residues will help increase the surface polarity of zein and also the resultant modified separators. The surface polarity of zein is first analyzed by measuring the water contact angle (WCA) in **Fig. 3d**. Interestingly, the separator coated by PRC-Zein displays a much larger WCA of 50˚ than that of SRC-

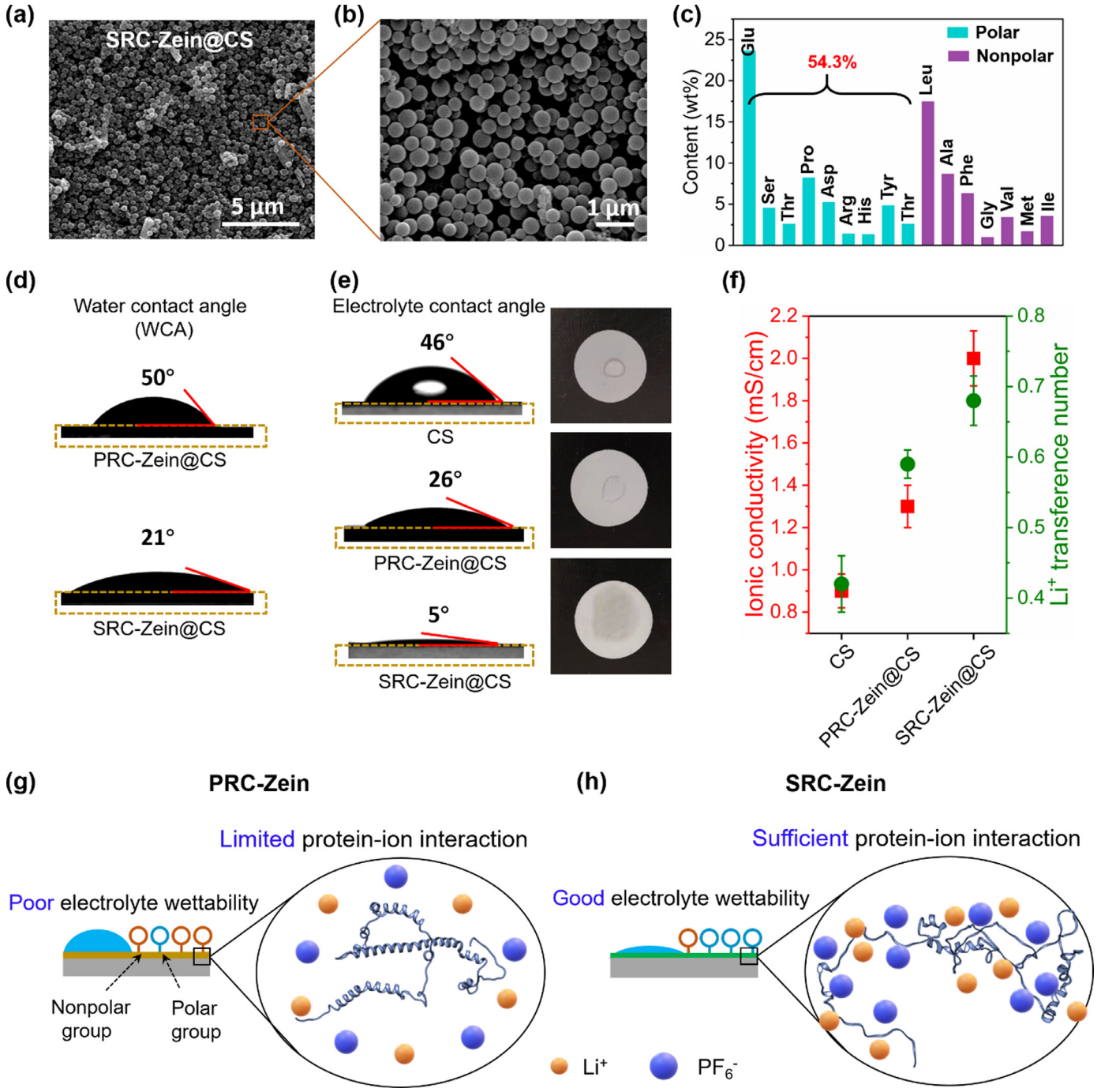


**Fig. 3.** Properties of zein with various configurations and the resulting modified separators. (a) – (b) SEM images of the SRC-Zein coated separator (SRC-Zein@CS). (c) Content of amino acids of zein. (d) Water contact angle (WCA) of zein modified separators. (e) Electrolyte contact angle of zein modified separators compared with a pristine commercial separator (CS), and digital photos of electrolyte droplets (20 μL) being dropped on the corresponding separators. (f) Summary of the ionic conductivity and $Li^+$ transference number of various separators. Schematics of electrolyte wettability and protein-ion interaction of (g) PRC-Zein@CS and (h) SRC-Zein@CS.

Zein (21°). This result implies that more polar residues are disclosed on the surface of SRC-Zein, leading to a significantly increased hydrophilicity. The unraveled polar residues also increase the wettability to the liquid electrolyte consisting of 1 M $LiPF_6$ dissolved in a mixture solvent of ethylene carbonate/ethyl methyl carbonate (v/v = 1/1). As presented in Fig. 3**e**, the uncoated separator, CS, shows a high electrolyte contact angle of 46° due to its hydrophobic nature. Modifying the separator surface with zein obviously increases the wettability for the electrolyte, but it is worth noting that SRC-Zein@CS shows a much better electrolyte affinity than that of PRC-Zein@CS: The electrolyte contact angle of SRC-Zein@CS is only 5° compared with 26° for PRC-Zein@CS. When 20 μL of the electrolyte is dropped on the separator surface, the electrolyte immediately spreads over SRC-Zein@CS. In contrast, PRC-Zein@CS shows slight wetting of the electrolyte droplet while the droplet maintains its shape without a significant change on CS. As a result, SRC-Zein@CS shows the highest electrolyte uptake of 134 ± 4.5%, compared with PRC-Zein@CS (128.4 ± 4.6%) and CS (98.7 ± 3.2%) in **Figure S8**.

It is well accepted that higher electrolyte wettability and higher electrolyte uptake will benefit the ionic conductivity due to the facilitated permeation and diffusion of the liquid electrolyte. Here, we surprisingly find that the SRC-Zein enhances not only the ionic conductivity, but also the $Li^+$ transference number, which is believed to be contributed by its unique molecular configuration. As shown in **Fig. 3f**, zein-modified separators present higher ionic conductivities than CS, owing to the improved electrolyte uptake/electrolyte wettability as discussed above. The ionic conductivities of SRC-Zein@CS, PRC-Zein@CS and CS are 2 ± 0.13, 1.3 ± 0.1, and 0.9 ± 0.08 mS/cm, respectively. It clearly shows that SRC-Zein@CS delivers the highest ionic conductivity, which is consistent with the electrolyte wettability results. Interestingly, the $Li^+$ transference number of SRC-Zein@CS is significantly increased to 0.68, which is much greater than that of PRC-Zein@CS (0.59) and CS (0.42) (see **Figure S9** and **Table S1** for the current-time evolution curves and calculation data). The simultaneously increased ionic conductivity and $Li^+$ transference number make a great contribution toward improving the electrochemical performance, especially the rate capability, and the effectiveness in stabilizing the Li anode.

In view of the above findings, we speculate that the molecular configurations of zein play an important role in the ionic interactions, making the significant differences in both $Li^+$ transference number and ionic conductivity. It is noted that when zein particles are dispersed in the electrolyte, they quickly precipitate from the electrolyte in **Figure S10**, indicating that the exposed functional groups play the most important role in the interactions with ions. As indicated by both molecular simulations and experimental studies before, the PRC-Zein shows a relatively compact molecular configuration and insufficient exposure of polar functional groups in **Fig. 3g**. Consequently, the improvements to both electrolyte wettability and ionic conductivity are limited. More importantly, as some polar groups, such as -$NH_2$, can form H-bonding with $PF_6^-$ [28–29] (see the schematic in **Figure S11**), activating these polar groups, that is, uncovering them from the embedded protein structure, is important for enhancing the anion-tethering strength. At the same time, the oxygen-containing groups (e.g., C=O and -COOH groups) have affinity with $Li^+$, such that adding a zein coating with the favorable configuration adjacent to the Li anode can increase the uniformity of the $Li^+$ flux and inhibit $Li^+$ movement toward the protrusions by the "tip effect" [49–50]. Therefore, regarding the PRC-Zein, the relatively close configuration leads to less access by both $Li^+$ and $PF_6^-$, resulting in a poorer tethering of $PF_6^-$ and a weaker affinity with $Li^+$. By a sharp contrast, the SRC-Zein reveals a more unfolded and more expansive configuration that leads to sufficient disclosure of polar functional groups. This leads to further improvement in the electrolyte wettability and ionic conductivity while also generating more active sites for tethering anions/interacting with $Li^+$ as illustrated in **Fig. 3h**. This significant difference will strongly impact the ability of the two configurations in stabilizing the Li anode, which will be discussed below.

To study the stability of the Li metal anode, Li/Cu half-cells are assembled with the zein modified separators. It is noted that the zein-coated side is placed facing the Cu electrode. As shown in **Fig. 4a**, the cell with the CS undergoes an obvious increase of the overpotential from ca. 200 h. The long-term plating/stripping stability is greatly improved by the zein-modified separators; the cells with PRC-Zein@CS or SRC-Zein@CS show stable and nearly constant overpotential. The Coulombic efficiency compared in **Fig. 4b** reflects the ratio of the stripped Li versus the plated Li and indicates the stability of the repeated Li plating/stripping processes [51–52]. As shown, the Li/Cu cell with the CS shows a rapid decay in the Coulombic efficiency that drops to 68.6% at the 77th cycle, which is due to the depletion of the Li and electrolyte by continuous formation/breakage of SEI layers [53–54]. The cells with SRC-Zein@CS or PRC-Zein@CS deliver more stable Coulombic efficiencies for 75 cycles. It is also found that, on average, the cell with the SRC-Zein@CS presents a higher Coulombic efficiency of 96.2% than that of the cell with the PRC-Zein@CS (91.4%). The detailed voltage profiles at various cycles are presented in **Fig. 4c-e**. The dips and bumps appear in the voltage curves of the CS cell, whereas the cells with zein modified separators present flatter plateaus. The results indicate that the zein modified separators deliver an easier and more stable insertion/extraction of Li [55]. The overpotential of the CS cell is significantly greater than that of the other two at various cycles and the stripping capacity obviously decays from 0.85 mAh/g at the 40th cycle to 0.81 mAh/g at the 60th cycle. The cell with SRC-Zein@CS shows similar overpotential with the PRC-Zein@CS counterpart, but the amount of stripped Li of it is much higher in comparison. For instance, at the 40th cycle, the capacities of stripped Li are 0.94 and 0.97 mAh/$cm^2$ for PRC-Zein@CS and SRC-Zein@CS, respectively. These results demonstrate that the SRC-Zein@CS is more conducive to regulate the stable plating/stripping of Li and reduce the loss of Li, thus more effectively increasing the Coulombic efficiencies, which is a primary challenge for LMBs.

To further investigate the interface evolution, the electrochemical impedance spectroscopy (EIS) at the 5$^{th}$ and the 50$^{th}$ cycle for the Li/Cu cells is conducted, the results of which are displayed in **Fig. 4f and g**. For fitting the EIS spectra, the equivalent circuit is used and shown in **Figure S12**. The initial interception with the X-axis is attributed to the bulk resistance ($R_b$). The semicircle can be assigned to the resistance of the passivation film on the Li anode surface ($R_{SEI}$) at high frequencies and the charge-transfer interfacial resistance ($R_{CT}$) at low frequencies [56]. As shown in **Fig. 4f**, at the 5th cycle, the $R_{CT}$ of the cells with the PRC-Zein@CS or the SRC-Zein@CS is 576.5 Ω and 371.5 Ω, respectively, which are much greater than that of the cell with the CS (226.1 Ω). This is because the zein coating layer enlarges the diffusion distance of the ions compared to the CS and the separator/electrode interface is not stable yet in the initial cycles. However, the $R_{CT}$ of the SRC-Zein@CS that obtains a higher ionic conductivity is still lower than that of the PRC-Zein@CS. At the 50th cycle (**Fig. 4g**), a notable change of both $R_{CT}$ and $R_{SEI}$ is observed for all of the Li/Cu cells. The $R_{SEI}$ of the cells with the CS, the PRC-Zein@CS, or the SRC-Zein@CS is 272.2, 45.2 and 3.3 Ω, respectively (see the fitting results in **Table S2**). The reduced $R_{SEI}$ of the two cells with the zein modified separators is caused by the improvements in both $Li^+$ transference number and ionic conductivity, which synergistically help the uniform deposition of $Li^+$. More specifically, the SRC-Zein@CS cell demonstrates the smallest $R_{SEI}$, indicating its exceptional ability in stabilizing the formation of thin SEI layer and the depression of Li dendrites compared with the PRC-Zein@CS. In addition, the $R_{CT}$ of the cell with the CS is considerably increased from 226.1 to 944.5 Ω. This is due to the excessive consumption of the electrolyte and the formation of a thick SEI layer with "dead" Li species that come from the repeated breakage/repair of SEI in the cyclic process. By contrast, the cells with the zein modified separators show a much lower $R_{CT}$ with less significant change upon cycling. The $R_{CT}$ of the PRC-Zein@CS cell is increased from 576.5 to 583.5 Ω. In comparison, the $R_{CT}$ of the SRC-Zein@CS cell is decreased from 371.5 to 331.6 Ω. The much lower $R_{CT}$ of the SRC-Zein@CS cell is attributed to the higher ionic conductivity and the thinner SEI layer, which simultaneously reduce the $R_{CT}$.

**Fig. 5** shows the morphologies of deposited Cu electrodes disassembled from the Li/Cu cells after certain cycles at 0.5 mA/$cm^2$. As shown in **Fig. 5a and b**, numerous Li dendrites grow on the Cu electrode with the CS from the 20th cycle. At the 50th cycle, the dendrites drastically proliferate during the repeated plating/stripping process, generating a great number of cracks and "dead" Li species in **Fig. 5b**. As depicted in **Fig. 5c**, in the cell with the CS, both the $Li^+$ transferability and the $Li^+$ flux uniformity are low. When the electrolyte diffuses through the CS having irregular pores, the ions tend to concentrate near the pores. Along with the poor surface polarity of the CS, the distribution of the $Li^+$ flux and the deposition of $Li^+$ on the anode surface are inhomogeneous, initiating the nucleation of Li dendrites from the beginning of the cyclic process. The uneven $Li^+$ flux tends to deposit on the "hot spots" of the SEI layer leading to uncontrollable growth of Li dendrites and SEI fracture, which is also known as "tip effect" [57]. In comparison, the morphologies of the Cu electrodes with the PRC-Zein@CS or the SRC-Zein@CS are much

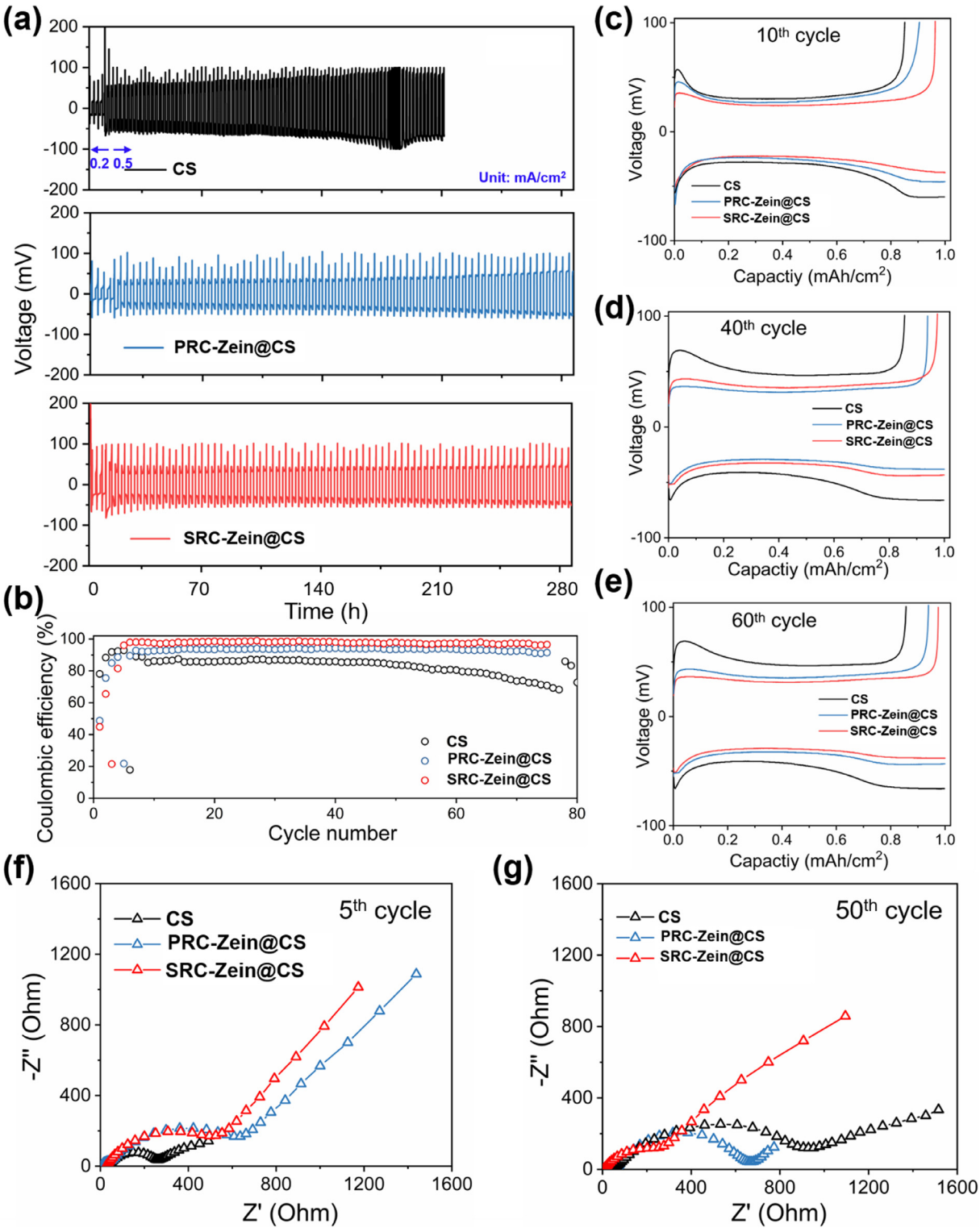


**Fig. 4.** Li plating/stripping performance of Li/Cu cells with various separators. (a) Voltage profiles of various separators. The current density is 0.5 mA/cm$^2$ and the Li deposition capacity is 1 mAh/cm$^2$. (b) Coulombic efficiency of Li/Cu cells with various separators. (c) – (e) Magnified voltage profiles of the Li/Cu cells at different cycles. (f) – (g) Nyquist plots of various Li/Cu cells at (f) the 5th cycle and (g) the 50th cycle.

smoother at the 20th cycle in Fig. 5**d and g**, because 1) the higher surface polarity and the rich lithiophilic groups (-C=O and -COOH) of zein redistribute and homogenize the $Li^+$ flux, avoiding the "tip effect" and helping the ion deposition in a more uniform manner, and 2) the higher $Li^+$ transference number due to the anionphilic group (-$NH_2$) of zein helps tether the anions and diminish the space-charge region to prolong the Sand's time and postpone the nucleation of Li dendrites [58]. These two factors effectively suppress the formation and growth of Li dendrites and contribute to a smoother and dendrite-free surface. However, for the Cu electrode with the PRC-Zein@CS, the dendrites start to nucleate at the 50$^{th}$ cycle in Fig. 5**e**, while the Cu electrode with the SRC-Zein@CS still shows a flat and dendrite-free surface in Fig. 5**h**. We

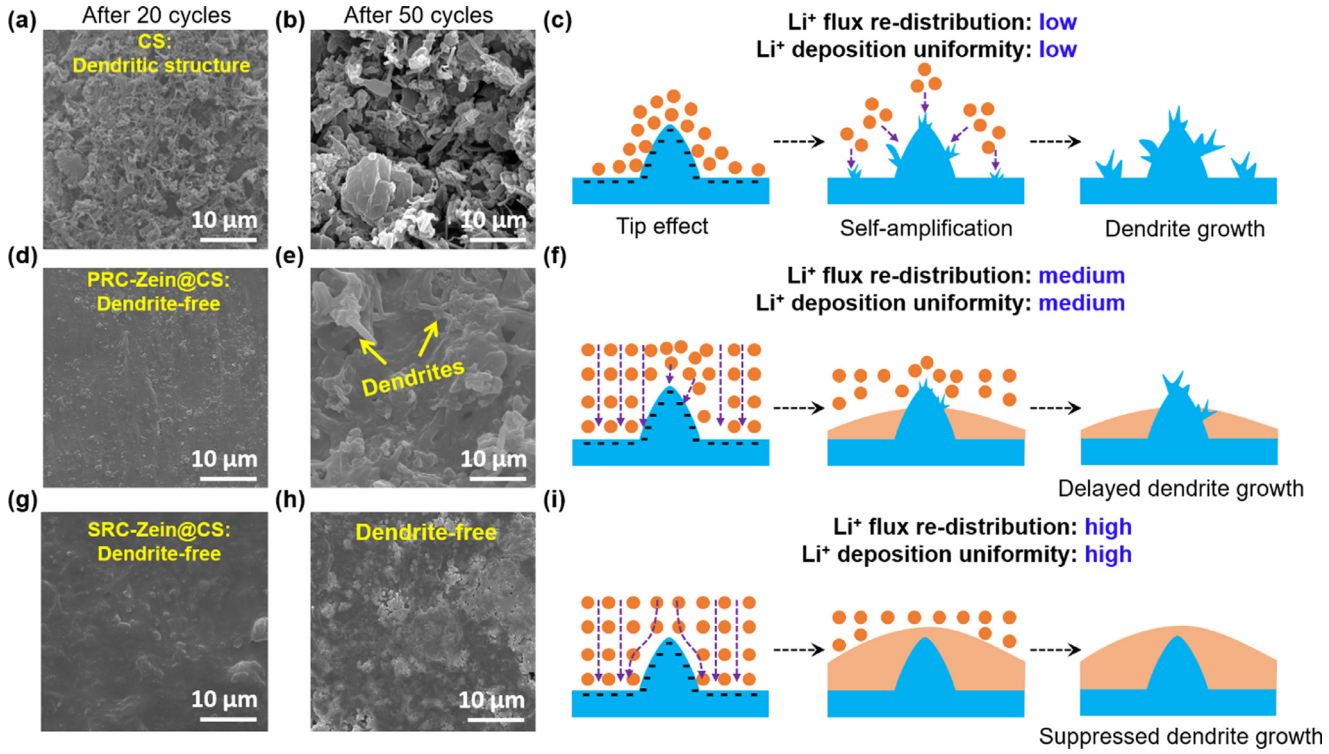


**Fig. 5.** Morphological studies of cycled Cu electrodes in deposition state. SEM images of the Cu electrode with CS after (a) 20 cycles and (b) 50 cycles. SEM images of the Cu electrode with PRC-Zein@CS after (d) 20 cycles and (e) 50 cycles. SEM images of the Cu electrode with SRC-Zein@CS after (g) 20 cycles and (h) 50 cycles. Schematics of Li deposition conditions for (c) CS, (f) PRC-Zein@CS and (i) SRC-Zein@CS.

recall that the PRC-Zein shows a limited exposure of lithiophilic polar groups (-C=O and -COOH), thus restricting the interactions with $Li^+$. In this case, there is still a likelihood that the $Li^+$ deposits toward the protrusions by the "tip effect", such that the regulation of the $Li^+$ flux distribution is weakened. Meanwhile, the reduced effectiveness in tethering anions further deteriorates the stability of ion deposition. Therefore, as shown in Fig. 5**f and i**, the PRC-Zein@CS makes a limited contribution to improving the $Li^+$ flux uniformity and the stability of $Li^+$ deposition compared with the SRC-Zein@CS. With the higher effectiveness in redistributing and homogenizing $Li^+$ flux, the deposition of $Li^+$ with the SRC-Zein@CS is well stabilized to strongly suppress the nucleation of Li dendrites. In contrast, the PRC-Zein@CS delays the growth of dendrites but it is not chronically effective. Because a high pressure is induced inside the coin cells, the morphology of the electrodes may be impacted. We also assemble beaker cells using Li foil and Cu foil as the electrodes and perform the plating/stripping test at 1 mA/cm$^2$ for 30 cycles with a capacity of 1 mAh/cm$^2$. As displayed in **Figure S13a**, numerous Li dendrites and "dead" Li species emerge for the pristine separator. This problem is alleviated by the zein modified separators; notably, less dendrites form for the SRC-Zein@CS than the PRC-Zein@CS, resulting in a very smooth and even Li surface (**Figure S13b and c**). The results are supplementary and consistent with the results obtained from the coin cells.

To further confirm the contributions of the SRC-Zein@CS to stabilizing the Li anode, symmetrical Li/Li cells are tested in Fig. 6. In Fig. 6**a**, the Li/Li cell with the CS shows a sharply increased overpotential from about the 350$^{th}$ hour and the overpotential keeps increasing afterwards. This is due to the gradual consumption of the electrolyte and Li, greatly increasing the cell resistance. The Li plating/stripping stability is greatly improved by the SRC-Zein@CS. Although in the first 80 h the overpotential slightly fluctuates, possibly because of the dissolution of the native passivation film on the Li metal surface, the overpotential becomes very stable for up to ca. 580 h. The magnified voltage profiles in Fig. 6**b and c** show that the SRC-Zein@CS cell generates flatter plateaus owing to the smooth and reversible ion deposition process. Meanwhile, the overpotential of the SRC-Zein@CS cell, which is 29 mV, is obviously lower than that of the CS cell (35 mV) in Fig. 6**c**. These results indicate that the SRC-Zein@CS can help guide uniform deposition of $Li^+$ in symmetrical Li/Li cells, resulting in a thinner SEI layer and less "dead" Li species as seen from **Figure S14**. The current rate is then elevated to 2 mA/cm$^2$ with a higher Li deposition capacity of 4 mAh/cm$^2$ to study the long-term performance of the SRC-Zein@CS. As shown in Fig. 6**d**, after stabilization of the Li/separator interface and the complete dissolution of the passivation film on Li anodes in about 30–40 h, the Li/Li cell delivers an ultra-stable cycling performance for more than 1400 h. The inset shows that the overpotential is stabilized at about 122 mV and there is negligible voltage fluctuation. The flat charge/discharge plateaus suggest a very stable and facilitated deposition/extraction of Li upon cycling. The good cycling performance results from the exceptional ionic conductivity and high $Li^+$ transference number brought from the SRC-Zein. The above studies indicate the importance of zein configurations in stabilizing the Li anode. In a word, a more expansive configuration with more polar groups (e.g., C=O, -$NH_2$, -COOH, etc.) exposed, leads to better effectiveness in 1) binding with $Li^+$ to increase the distribution uniformity of $Li^+$ flux, and 2) tethering $PF_6^-$ to diminish the space-charge region at the anode surface. These two factors synergistically contribute to an even distribution of $Li^+$ flux and stable deposition of $Li^+$, which inhibit the nucleation of Li dendrites. The surface chemistry of the cycled Li is analyzed by XPS in **Figure S15** to reveal the SEI composition. The high-resolution F 1s spectra indicate that the LiF contents for CS and SRC-Zein@CS are very close, which are 50.9% and 51.7%, respectively. It is known that LiF is the main product from hydrolysis decomposition of $LiPF_6$ [59]. Therefore, the addition of the protein coating layer generates insignificant impact on the decomposition of $LiPF_6$ despite of the presence of polar groups.

The feasibility of the zein modified separators working in batteries is examined based on LMO/Li half-cells. Fig. 7**a** shows the typical charge/discharge voltage profiles of the LMO half cells at 0.1C. The cells

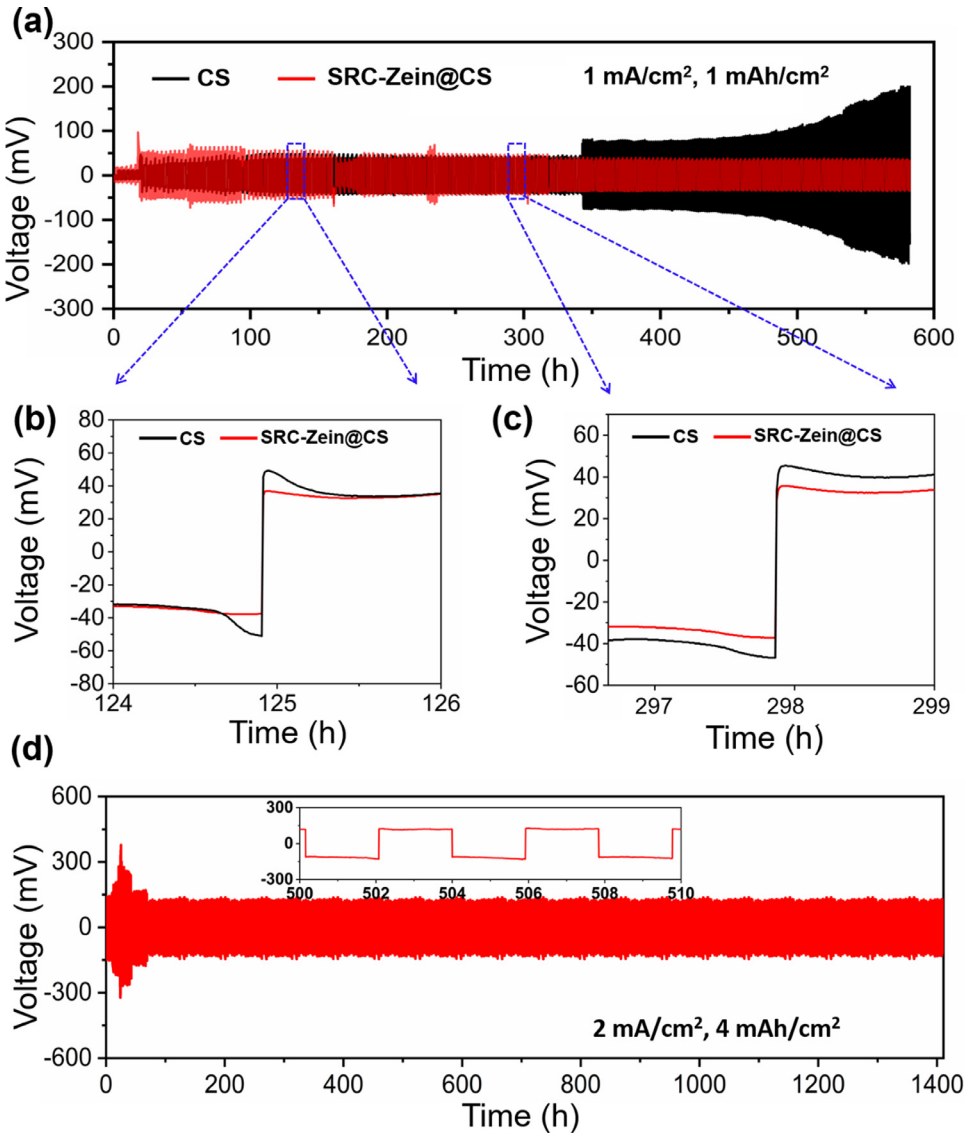


**Fig. 6.** Li plating/stripping performance of symmetrical Li/Li cells with various separators. (a) Voltage profiles of Li/Li cells with SRC-Zein@CS compared with CS at a current density of 1 mA/cm$^2$. (b) – (c) Magnified voltage profiles. (d) Voltage profiles of Li/Li cell with SRC-Zein@CS at a current density of 2 mA/cm$^2$.

with the CS, the PRC-Zein@CS, or the SRC-Zein@CS deliver initial discharge capacities of 129, 137 and 141 mAh/g, respectively. The highest capacity from the SRC-Zein@CS is attributed to its exceptional ionic conductivity that facilitates the transfer of $Li^+$. In addition, the rate performance in Fig. 7**b** demonstrates that the cells with the PRC-Zein@CS or the SRC-Zein@CS show markedly higher capacities than that of the cell with the CS in all current rates, especially at 2C. It is also noted that the SRC-Zein@CS cell outmatches the PRC-Zein@CS cell. A high discharge capacity of 102 mAh/g at 1C is achieved by SRC-Zein@CS, which is higher than that of the PRC-Zein@CS Cell (97 mAh/g). The corresponding capacity of the CS cell is only 91 mAh/g. After reducing the current from 2C to 0.2C, a capacity of 123 mAh/g can be recovered by the SRC-Zein@CS, while the corresponding capacities are 116 and 109 mAh/g for the PRC-Zein@CS and the CS, respectively. The cyclic voltammetry (CV) curves of the SRC-Zein@CS cell are presented in **Figure S16**. The CV curves at various scan rates show two pairs of well-defined redox peaks, suggesting that the insertion/de-insertion of $Li^+$ is a two-step process [60]. The curves at various cycles are highly reversible and there are no additional peaks emerging, which indicates the good electrochemical stability of zein in the continuous cyclic process.

The cycling stability of the LMO/Li cells is shown in Fig. 7**c**. Among the three cells, the SRC-Zein@CS cell presents the highest capacity for 400 cycles, followed by the PRC-Zein@CS and the CS cells. The initial capacities of the PRC-Zein@CS and SRC-Zein@CS cells are 109 and 119 mAh/g and the capacities of them at the 400th cycle are 66 and 95 mAh/g, respectively. Besides the higher capacity, the capacity retention of the cell with the SRC-Zein@CS (79.8%) is also much higher than that of the PRC-Zein@CS cell (60.6%). The interfacial evolution of the half-cells during cycling are analyzed by EIS in Fig. 7**d and e**. The equivalent circuit can be found in **Figure S12**. The semicircle in the EIS spectra includes the $R_{SEI}$ and $R_{CT}$ at high and medium frequencies, respectively. It can be seen that both the $R_{SEI}$ and $R_{CT}$ undergo dynamic changes during cycling. According to the fitting results in **Table S3**, for the cell with the CS, the $R_{SEI}$ keeps increasing from 6.5 Ω (fresh cell) to 25.7 Ω at the 5th cycle, then to 45.2 Ω at the 50th cycle. This indicates that the SEI layer constantly accumulates along with repeated cycling process because the uneven ion deposition induces unstable formation of the SEI layer. Accordingly, the $R_{CT}$ enlarges from 227.7 Ω to 299.6 Ω from the 5th to the 50th cycle due to the thickening SEI layer and the formation of "dead" Li species. On the contrary, the evolution of both $R_{SEI}$ and $R_{CT}$ is less obvious for the cell with the SRC-Zein@CS. Through operation over 5 cycles, the $R_{SEI}$ remains stable and slightly decreases to 4.5 Ω compared with 5.6 Ω for the fresh cell. After cycling for 50 cycles, the $R_{SEI}$ is 25.7 Ω, which is much smaller than that of the cell with the CS. The results reveal that the SRC-Zein@CS cell obtains a much thinner SEI layer, attributed to the more stable ion

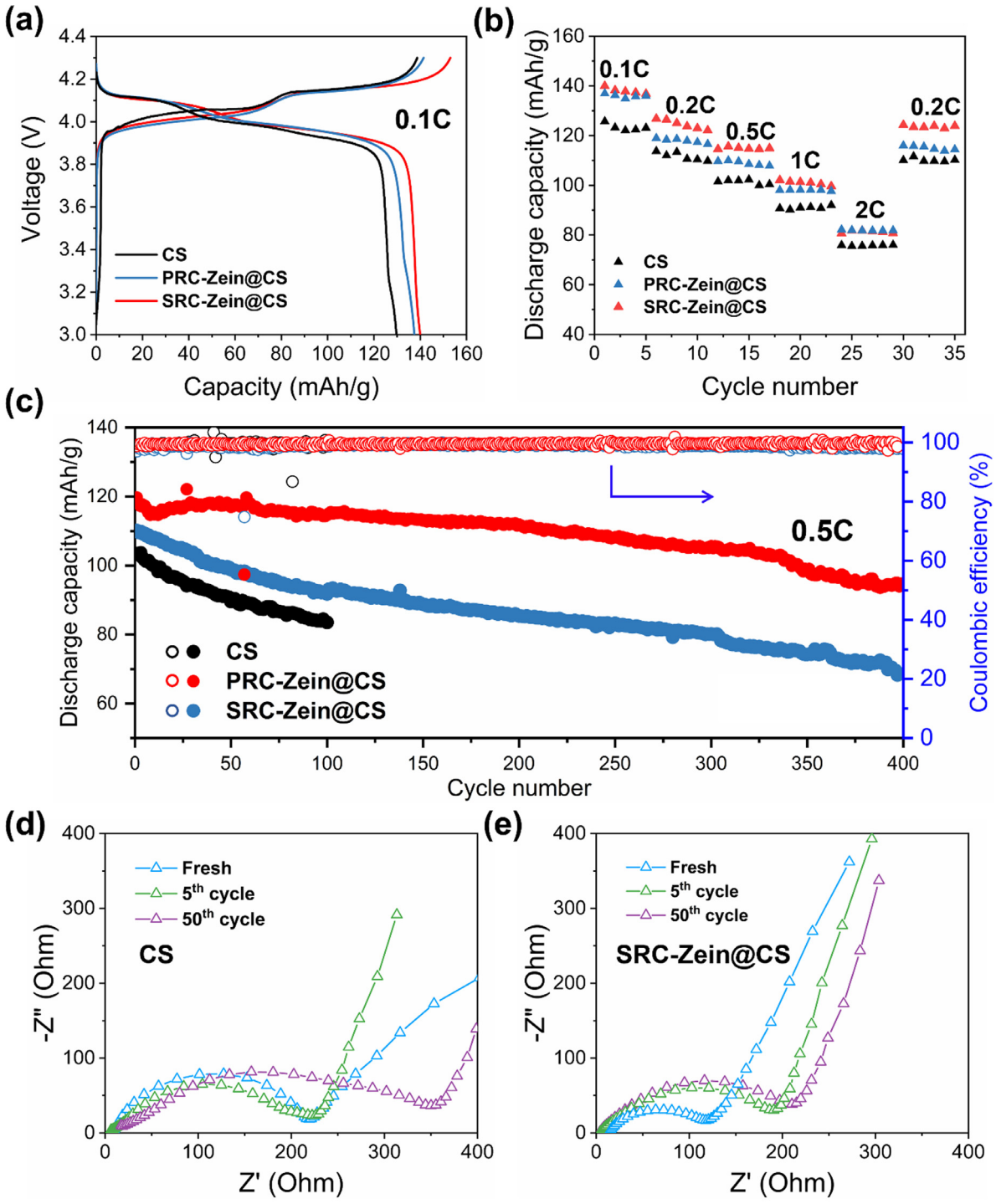


**Fig. 7.** Electrochemical performance of various separators in $LiMn_2O_4$/Li (LMO/Li) half-cells. (a) Voltage profiles of various separators at 0.1C. (b) Rate performance of various separators. (c) Cycle stability of various separators tested at 0.5C. (d) – (e) Nyquist plots of the half cells with (d) CS and (e) SRC-Zein@CS at 0.5C.

deposition that protects the SEI layer against breakage. In addition, the $R_{CT}$ visibly grows in the first 5 cycles from 121.9 Ω to 164.5 Ω, which is, however, stabilized afterwards, remaining nearly constant at the 50$^{th}$ cycle (163.1 Ω). The results indicate that the SRC-Zein@CS cell has a more stable and faster transfer of $Li^+$ than the CS cell. When increasing the loading level of LMO to 6.8 mg/cm$^2$, the cells with zein modified separators still outperform that with a pristine separator. As shown in **Figure S17a**, the three cells demonstrate typical LMO voltage profiles and the SRC-Zein@CS cell shows the highest discharge capacity of 133 mAh/g at the first cycle; the discharge capacities of the cells with CS and PRC-Zein@CS are 120 and 126 mAh/g, respectively. At varying current rates (**Figure S17b**), the PRC-Zein@CS cell delivers the highest capacities, which further proves it advantages in improving the battery performance.

The cycled Li anodes are collected from the LMO/Li half-cells having been operated for 200 cycles at 0.5C and their surface morphologies are examined. As shown in **Figure S18a**, the Li anode with the CS shows many visible Li dendrites as circled, while the surface of the Li anode with the SRC-Zein@CS is much smoother in **Figure S18b**. These results are consistent with the EIS data that the SRC-Zein@CS successfully sup-

presses the Li dendrites and "dead" Li species, and stabilizes the SEI layer in LMO/Li half-cells during charge/discharge cycling. Furthermore, it is well known that the dissolution of Mn ions from the LMO leads to the capacity fading and Li anode corrosion/passivation.[61–62] We explore that the zein layer shows some capability to adsorb Mn ions to depress the deposition of Mn ions on the Li anode. **Figure S19** displays the inductively coupled plasma-optical emission spectrometry (ICP-OES) result, showing the concentration of $Mn^{2+}$ of $MnCl_2$ solution before and after a specific amount of zein is soaked in the solution for 1 hour. As shown, the concentration of $Mn^{2+}$ is decreased by 57.1 mg/L after the soaking of zein, which indicates that zein is able to adsorb $Mn^{2+}$ to provide further protection for the Li anode.

## 3. Conclusion

In summary, we explore a natural "relief" for Li dendrites, zein protein, and exploit it to functionalize the separator to achieve stable and long-life Li metal anodes. It is found through experiments and molecular simulations that the dendrite-suppressing strength of zein is sensitive to its molecular configurations. With the use of a vigorous denaturant, aq. HAc, the protein structure is drastically unfolded and opened, strengthening the exposure of polar residues and the protein-ion interactions. The generated "strong relief configuration" (SRC-Zein), being coated on the separator, leads to a better electrolyte wettability, higher ionic conductivity (2.0 mS/cm), and higher $Li^+$ transference number (0.68) than the less unfolded zein. Benefiting from these significant properties, the SRC-Zein effectively stabilizes the ion deposition and suppresses the nucleation/growth of Li dendrites. The resulting Li/Cu cell and symmetrical Li/Li cell both deliver stable performance and prolonged cycle life; particularly, the symmetrical Li/Li cell demonstrates remarkable cycling stability for more than 1400 h at 2 mA/cm$^2$. In addition, the capacity, cycling stability, and rate performance of the LMO/Li cell are all improved by the SRC-Zein, proving its feasibility to stabilize the Li anode in LMBs. This study provides a new insight into tailoring the structures and functions of natural proteins to generate advanced interfacial materials that address the critical challenges of LMBs.

## Declaration of competing Interest

The authors declare that they have no known competing financial interests or personal relationships that could have appeared to influence the work reported in this paper.

## CRediT authorship contribution statement

**Xuewei Fu:** Conceptualization, Methodology, Investigation, Writing – original draft, Writing – review & editing. **Ryan Odstrcil:** Methodology, Formal analysis, Writing – original draft, Writing – review & editing. **Munan Qiu:** Investigation. **Jin Liu:** Supervision, Funding acquisition. **Wei-Hong Zhong:** Supervision, Funding acquisition, Writing – review & editing.

## Acknowledgements

The authors would like to acknowledge the financial support by NSF CBET 1929236. Computational resources were provided in part by the Extreme Science and Engineering Discovery Environment (XSEDE) under grant No. MCB170012. Dr. Munan Qiu was sponsored by the China Scholarship Council for her visit at Washington State University. The authors also appreciate the support on microscopy characterizations from the Franceschi Microscopy & Imaging Center at Washington State University.

## Supplementary materials

Supplementary material associated with this article can be found, in the online version, at doi:10.1016/j.ensm.2021.07.010.

## References

[1] Y. Guo, H. Li, T. Zhai, Reviving lithium-metal anodes for next-generation high-energy batteries, Adv. Mater. 29 (29) (2017) 1700007, doi:10.1002/adma.201700007.
[2] C. Wang, A. Wang, L. Ren, X. Guan, D. Wang, A. Dong, C. Zhang, G. Li, J Luo, Controlling Li ion flux through materials innovation for dendrite-free lithium metal anodes, Adv. Funct. Mater. 29 (49) (2019) 1905940, doi:10.1002/adfm.201905940.
[3] X. Gao, Y.-N. Zhou, D. Han, J. Zhou, D. Zhou, W. Tang, J.B. Goodenough, Thermodynamic understanding of Li-dendrite formation, Joule 4 (9) (2020) 1864–1879, doi:10.1016/j.joule.2020.06.016.
[4] G. Yasin, M. Arif, T. Mehtab, X. Lu, D. Yu, N. Muhammad, M.T. Nazir, H. Song, Understanding and suppression strategies toward stable Li metal anode for safe lithium batteries, Energy Storage Mater. 25 (2020) 644–678, doi:10.1016/j.ensm.2019.09.020.
[5] A. Wang, S. Kadam, H. Li, S. Shi, Y. Qi, Review on modeling of the anode solid electrolyte interphase (SEI) for lithium-ion batteries, NPJ Comput. Mater. 4 (1) (2018) 15, doi:10.1038/s41524-018-0064-0.
[6] N.-W. Li, Y.-X. Yin, J.-Y. Li, C.-H. Zhang, Y.-G. Guo, Passivation of lithium metal anode via hybrid ionic liquid electrolyte toward stable Li plating/stripping, Adv. Sci. 4 (2) (2017) 1600400, doi:10.1002/advs.201600400.
[7] W. Ren, C. Ding, X. Fu, Y. Huang, Advanced gel polymer electrolytes for safe and durable lithium metal batteries: challenges, strategies, and perspectives, Energy Storage Mater. 34 (2021) 515–535, doi:10.1016/j.ensm.2020.10.018.
[8] C. Ding, X. Fu, H. Li, J. Yang, J.-L. Lan, Y. Yu, W.-H. Zhong, X. Yang, An ultrarobust composite gel electrolyte stabilizing ion deposition for long-life lithium metal batteries, Adv. Funct. Mater. 29 (43) (2019) 1904547, doi:10.1002/adfm.201904547.
[9] X. Chen, Y. Lv, M. Shang, J. Niu, Ironing controllable lithium into lithiotropic carbon fiber fabric: a novel Li-metal anode with improved cyclability and dendrite suppression, ACS Appl. Mater. Interfaces 11 (24) (2019) 21584–21592, doi:10.1021/acsami.9b05364.
[10] D. Zhang, A. Dai, M. Wu, K. Shen, T. Xiao, G. Hou, J. Lu, Y. Tang, Lithiophilic 3D porous CuZn current collector for stable lithium metal batteries, ACS Energy Lett. 5 (1) (2020) 180–186, doi:10.1021/acsenergylett.9b01987.
[11] C.-P. Yang, Y.-X. Yin, S.-F. Zhang, N.-W. Li, Y.-G. Guo, Accommodating lithium into 3D current collectors with a submicron skeleton towards long-life lithium metal anodes, Nat. Commun. 6 (1) (2015) 8058, doi:10.1038/ncomms9058.
[12] W. Zhou, S. Wang, Y. Li, S. Xin, A. Manthiram, J.B. Goodenough, Plating a dendrite-free lithium anode with a polymer/ceramic/polymer sandwich electrolyte, J. Am. Chem. Soc. 138 (30) (2016) 9385–9388, doi:10.1021/jacs.6b05341.
[13] D. Wang, W. Zhang, W. Zheng, X. Cui, T. Rojo, Q. Zhang, Towards high-safe lithium metal anodes: suppressing lithium dendrites via tuning surface energy, Adv. Sci. 4 (1) (2017) 1600168, doi:10.1002/advs.201600168.
[14] W. Liu, Y. Mi, Z. Weng, Y. Zhong, Z. Wu, H. Wang, Functional metal–organic framework boosting lithium metal anode performance via chemical interactions, Chem. Sci. 8 (6) (2017) 4285–4291, doi:10.1039/C7SC00668C.
[15] K. Wang, L. Yang, Z. Wang, Y. Zhao, Z. Wang, L. Han, Y. Song, F. Pan, Enhanced lithium dendrite suppressing capability enabled by a solid-like electrolyte with different-sized nanoparticles, Chem. Commun. 54 (93) (2018) 13060–13063, doi:10.1039/C8CC07476C.
[16] J.-H. Han, E. Khoo, P. Bai, M.Z. Bazant, Over-limiting current and control of dendritic growth by surface conduction in nanopores, Sci. Rep. 4 (1) (2014) 7056, doi:10.1038/srep07056.
[17] J.-K. Kim, D.H. Kim, S.H. Joo, B. Choi, A. Cha, K.M. Kim, T.-H. Kwon, S.K. Kwak, S.J. Kang, J. Jin, Hierarchical chitin fibers with aligned nanofibrillar architectures: a nonwoven-mat separator for lithium metal batteries, ACS Nano 11 (6) (2017) 6114–6121, doi:10.1021/acsnano.7b02085.
[18] T. Zhang, J. Yang, Z. Xu, H. Li, Y. Guo, C. Liang, J. Wang, Suppressing dendrite growth of a lithium metal anode by modifying conventional polypropylene separators with a composite layer, ACS Appl. Energy Mater. 3 (1) (2020) 506–513, doi:10.1021/acsaem.9b01763.
[19] Y. Liu, S. Xiong, J. Wang, X. Jiao, S. Li, C. Zhang, Z. Song, J. Song, Dendrite-free lithium metal anode enabled by separator engineering via uniform loading of lithiophilic nucleation sites, Energy Storage Mater. 19 (2019) 24–30, doi:10.1016/j.ensm.2018.10.015.
[20] C.-Z. Zhao, X.-Q. Zhang, X.-B. Cheng, R. Zhang, R. Xu, P.-Y. Chen, H.-J. Peng, J.-Q. Huang, Q. Zhang, An anion-immobilized composite electrolyte for dendrite-free lithium metal anodes, in: Proceedings of the National Academy of Sciences, 2017, doi:10.1073/pnas.1708489114.
[21] M.D. Tikekar, S. Choudhury, Z. Tu, L.A. Archer, Design principles for electrolytes and interfaces for stable lithium-metal batteries, Nat. Energy 1 (9) (2016) 16114, doi:10.1038/nenergy.2016.114.
[22] H. Huo, X. Li, Y. Chen, J. Liang, S. Deng, X. Gao, K. Doyle-Davis, R. Li, X. Guo, Y. Shen, C.-W. Nan, X. Sun, Bifunctional composite separator with a solid-state-battery strategy for dendrite-free lithium metal batteries, Energy Storage Mater. 29 (2020) 361–366, doi:10.1016/j.ensm.2019.12.022.
[23] X. Mao, L. Shi, H. Zhang, Z. Wang, J. Zhu, Z. Qiu, Y. Zhao, M. Zhang, S. Yuan, Polyethylene separator activated by hybrid coating improving Li+ ion transference number and ionic conductivity for Li-metal battery, J. Power Sources 342 (2017) 816–824, doi:10.1016/j.jpowsour.2017.01.006.
[24] X. Fu, W.-H. Zhong, Biomaterials for high-energy lithium-based batteries: strategies, challenges, and perspectives, Adv. Energy Mater. 9 (40) (2019) 1901774, doi:10.1002/aenm.201901774.
[25] C. Liedel, Sustainable battery materials from biomass, ChemSusChem 13 (9) (2020) 2110–2141, doi:10.1002/cssc.201903577.

[26] J. Wan, J. Zhang, J. Yu, J. Zhang, Cellulose aerogel membranes with a tunable nanoporous network as a matrix of gel polymer electrolytes for safer lithium-ion batteries, ACS Appl. Mater. Interfaces 9 (29) (2017) 24591–24599, doi:10.1021/acsami.7b06271.
[27] D. Xu, B. Wang, Q. Wang, S. Gu, W. Li, J. Jin, C. Chen, Z. Wen, High-strength internal cross-linking bacterial cellulose-network-based gel polymer electrolyte for dendrite-suppressing and high-rate lithium batteries, ACS Appl. Mater. Interfaces 10 (21) (2018) 17809–17819, doi:10.1021/acsami.8b00034.
[28] A. Song, Y. Huang, X. Zhong, H. Cao, B. Liu, Y. Lin, M. Wang, X. Li, Novel lignocellulose based gel polymer electrolyte with higher comprehensive performances for rechargeable lithium–sulfur battery, J. Membr. Sci. 556 (2018) 203–213, doi:10.1016/j.memsci.2018.04.003.
[29] H. Wu, Q. Wu, F. Chu, J. Hu, Y. Cui, C. Yin, C. Li, Sericin protein as a conformal protective layer to enable air-endurable Li metal anodes and high-rate Li-S batteries, J. Power Sources 419 (2019) 72–81, doi:10.1016/j.jpowsour.2019.02.033.
[30] T. Wang, Y. Li, J. Zhang, K. Yan, P. Jaumaux, J. Yang, C. Wang, D. Shanmukaraj, B. Sun, M. Armand, Y. Cui, G. Wang, Immunizing lithium metal anodes against dendrite growth using protein molecules to achieve high energy batteries, Nat. Commun. 11 (1) (2020) 5429, doi:10.1038/s41467-020-19246-2.
[31] T.R. Hvidsten, A. Laegreid, A. Kryshtafovych, G. Andersson, K. Fidelis, J. Komorowski, A comprehensive analysis of the structure-function relationship in proteins based on local structure similarity, PLoS One 4 (7) (2009) e6266–e6266, doi:10.1371/journal.pone.0006266.
[32] W Widłak, Protein structure and function, in: W. Widłak (Ed.), Molecular Biology: Not Only for Bioinformaticians, Springer Berlin Heidelberg, Berlin, Heidelberg, 2013, pp. 15–29.
[33] G.W. Selling, S.A.H. Hamaker, D.J. Sessa, Effect of solvent and temperature on secondary and tertiary structure of Zein by circular dichroism, Cereal Chem. 84 (3) (2007) 265–270, doi:10.1094/CCHEM-84-3-0265.
[34] J.A. Lopez-Valenzuela, B.C. Gibbon, D.R. Holding, B.A. Larkins, Cytoskeletal proteins are coordinately increased in maize genotypes with high levels of eEF1A, Plant Physiol. 135 (3) (2004) 1784–1797, doi:10.1104/pp.104.042259.
[35] H.K. Frensdorff, M.T. Watson, W. Kauzmann, The kinetics of protein denaturation. IV. The viscosity and gelation of urea solutions of ovalbumin1, J. Am. Chem. Soc. 75 (21) (1953) 5157–5166, doi:10.1021/ja01117a004.
[36] M.L. Anson, A.E. Mirsky, The effect of denaturation on the viscosity of protein systems, J. Gen. Physiol. 15 (3) (1932) 341–350, doi:10.1085/jgp.15.3.341.
[37] Y. Feng, Y. Lee, Microfluidic fabrication of hollow protein microcapsules for rate-controlled release, RSC Adv. 7 (78) (2017) 49455–49462, doi:10.1039/C7RA08645H.
[38] Y. Miao, R. Yang, D.Y.B. Deng, L.-M. Zhang, Poly(l-lysine) modified zein nanofibrous membranes as efficient scaffold for adhesion, proliferation, and differentiation of neural stem cells, RSC Adv. 7 (29) (2017) 17711–17719, doi:10.1039/C7RA00189D.
[39] C. Ding, Y. Guo, J. Liu, G.B. Kent, B.T. Jobson, X. Fu, X. Yang, W.-H. Zhong, A super-breathable “woven-like” protein nanofabric, ACS Appl.Bio Mater. 3 (5) (2020) 2958–2964, doi:10.1021/acsabm.0c00008.
[40] G.W. Nelson, M. Perry, S.-M. He, D.L. Zechel, J.H. Horton, Characterization of covalently bonded proteins on poly(methyl methacrylate) by X-ray photoelectron spectroscopy, Colloids Surf. B 78 (1) (2010) 61–68, doi:10.1016/j.colsurfb.2010.02.012.
[41] S. Konno, T. Namiki, K. Ishimori, Quantitative description and classification of protein structures by a novel robust amino acid network: interaction selective network (ISN), Sci. Rep. 9 (1) (2019) 16654, doi:10.1038/s41598-019-52766-6.
[42] P.D. Sun, C.E. Foster, J.C. Boyington, Overview of protein structural and functional folds, Curr. Protoc. Protein Sci. Chapter 17 (1) (2004) 1711–17.1, doi:10.1002/0471140864.ps1701s35.
[43] X. Fan, Y. Wang, M. Zheng, F. Dunne, T. Liu, X. Fu, L. Kong, S. Pan, W.-H. Zhong, Morphology engineering of protein fabrics for advanced and sustainable filtration, J. Mater. Chem. A 6 (43) (2018) 21585–21595, doi:10.1039/C8TA08717B.
[44] L.A. Forato, T.D.C. Bicudo, L.A. Colnago, Conformation of $\alpha$ zeins in solid state by Fourier transform IR, Biopolymers 72 (6) (2003) 421–426, doi:10.1002/bip.10481.
[45] S. Ali, Z. Khatri, K.W. Oh, I.-S. Kim, S.H. Kim, Zein/cellulose acetate hybrid nanofibers: Electrospinning and characterization, Macromol. Res. 22 (9) (2014) 971–977, doi:10.1007/s13233-014-2136-4.
[46] L. Nie, Y. Li, S. Chen, K. Li, Y. Huang, Y. Zhu, Z. Sun, J. Zhang, Y. He, M. Cui, S. Wei, F. Qiu, C. Zhong, W. Liu, Biofilm nanofiber-coated separators for dendrite-free lithium metal anode and ultrahigh-rate lithium batteries, ACS Appl. Mater. Interfaces 11 (35) (2019) 32373–32380, doi:10.1021/acsami.9b08656.
[47] Y. Yang, B. Li, L. Li, S. Seeger, J. Zhang, A SuperLEphilic/Superhydrophobic and Thermostable Separator Based on Silicone Nanofilaments for Li Metal Batteries, iScience 16 (2019) 420–432, doi:10.1016/j.isci.2019.06.010.
[48] C. Man, P. Jiang, K.-w. Wong, Y. Zhao, C. Tang, M. Fan, W.-m. Lau, J. Mei, S. Li, H. Liu, D. Hui, Enhanced wetting properties of a polypropylene separator for a lithium-ion battery by hyperthermal hydrogen induced cross-linking of poly(ethylene oxide), J. Mater. Chem. A 2 (30) (2014) 11980–11986, doi:10.1039/C4TA01870B.
[49] C.-H. Chang, S.-H. Chung, A. Manthiram, Dendrite-free lithium anode via a homogenous Li-ion distribution enabled by a Kimwipe paper, Adv. Sustain. Syst. 1 (1–2) (2017) 1600034, doi:10.1002/adsu.201600034.
[50] Z. Liang, G. Zheng, C. Liu, N. Liu, W. Li, K. Yan, H. Yao, P.-C. Hsu, S. Chu, Y. Cui, Polymer nanofiber-guided uniform lithium deposition for battery electrodes, Nano Lett. 15 (5) (2015) 2910–2916, doi:10.1021/nl5046318.
[51] X. Fu, Y. Wang, L. Scudiero, W.-H. Zhong, A polymeric nanocomposite interlayer as ion-transport-regulator for trapping polysulfides and stabilizing lithium metal, Energy Storage Mater. 15 (2018) 447–457, doi:10.1016/j.ensm.2018.06.025.
[52] B.D. Adams, J. Zheng, X. Ren, W. Xu, J.-G. Zhang, Accurate determination of coulombic efficiency for lithium metal anodes and lithium metal batteries, Adv. Energy Mater. 8 (7) (2018) 1702097, doi:10.1002/aenm.201702097.
[53] F. Liu, R. Xu, Z. Hu, S. Ye, S. Zeng, Y. Yao, S. Li, Y. Yu, Regulating lithium nucleation via CNTs modifying carbon cloth film for stable Li metal anode, Small 15 (5) (2019) 1803734, doi:10.1002/smll.201803734.
[54] Z. Zhang, Y. Jin, Y. Zhao, J. Xu, B. Sun, K. Liu, H. Lu, N. Lv, Z. Dang, H. Wu, Homogenous lithium plating/stripping regulation by a mass-producible Zn particles modified Li-metal composite anode, Nano Res. (2021), doi:10.1007/s12274-021-3326-y.
[55] Z. Liang, D. Lin, J. Zhao, Z. Lu, Y. Liu, C. Liu, Y. Lu, H. Wang, K. Yan, X. Tao, Y. Cui, Composite lithium metal anode by melt infusion of lithium into a 3D conducting scaffold with lithiophilic coating, Proc. Natl. Acad. Sci. 113 (11) (2016) 2862, doi:10.1073/pnas.1518188113.
[56] S. Xia, J. Lopez, C. Liang, Z. Zhang, Z. Bao, Y. Cui, W. Liu, High-rate and large-capacity lithium metal anode enabled by volume conformal and self-healable composite polymer electrolyte, Adv. Sci. 6 (9) (2019) 1802353, doi:10.1002/advs.201802353.
[57] W. Liu, D. Lin, A. Pei, Y. Cui, Stabilizing lithium metal anodes by uniform Li-ion flux distribution in nanochannel confinement, J. Am. Chem. Soc. 138 (47) (2016) 15443–15450, doi:10.1021/jacs.6b08730.
[58] Y. Xu, T. Li, L. Wang, Y. Kang, Interlayered dendrite-free lithium plating for high-performance lithium-metal batteries, Adv. Mater. 31 (29) (2019) 1901662, doi:10.1002/adma.201901662.
[59] J.-G. Han, K. Kim, Y. Lee, N.-S. Choi, Scavenging materials to stabilize LiPF6-containing carbonate-based electrolytes for Li-ion batteries, Adv. Mater. 31 (20) (2019) 1804822, doi:10.1002/adma.201804822.
[60] X. Tang, B. Lin, Y. Ge, Y. Ge, C. Lu, S.V. Savilov, S.M. Aldoshin, H. Xia, $LiMn_2O_4$ nanorod arrays: a potential three-dimensional cathode for lithium-ion microbatteries, Mater. Res. Bull. 69 (2015) 2–6, doi:10.1016/j.materresbull.2014.11.020.
[61] M. Zhu, J. Wu, W.-H. Zhong, J. Lan, G. Sui, X. Yang, A biobased composite gel polymer electrolyte with functions of lithium dendrites suppressing and manganese ions trapping, Adv. Energy Mater. 8 (11) (2018) 1702561, doi:10.1002/aenm.201702561.
[62] T. Liu, A. Dai, J. Lu, Y. Yuan, Y. Xiao, L. Yu, M. Li, J. Gim, L. Ma, J. Liu, C. Zhan, L. Li, J. Zheng, Y. Ren, T. Wu, R. Shahbazian-Yassar, J. Wen, F. Pan, K. Amine, Correlation between manganese dissolution and dynamic phase stability in spinel-based lithium-ion battery, Nat. Commun. 10 (1) (2019) 4721, doi:10.1038/s41467-019-12626-3.